



Communication

# Hot Electrons, Hot Holes, or Both? Tandem Synthesis of Imines Driven by the Plasmonic Excitation in Au/CeO<sub>2</sub> Nanorods

Ivo F. Teixeira <sup>1,\*</sup>, Mauricio S. Homsí <sup>2</sup>, Rafael S. Geonmonond <sup>2</sup>, Guilherme F. S. R. Rocha <sup>2</sup>, Yung-Kang Peng <sup>3</sup>, Ingrid F. Silva <sup>4</sup>, Jhon Quiroz <sup>5</sup> and Pedro H. C. Camargo <sup>2,5,\*</sup>

<sup>1</sup> Department of Chemistry, Federal University of São Carlos, São Carlos 13565-905, Brazil

<sup>2</sup> Department of Fundamental Chemistry, Institute of Chemistry, University of São Paulo, São Paulo 05508-000, Brazil; mauriciosamuel.homsí@usp.br (M.S.H.); rafaelsg31@gmail.com (R.S.G.); guilhermefrocha@gmail.com (G.F.S.R.R.)

<sup>3</sup> Department of Chemistry, City University of Hong Kong, Yeung Kin Man Academic Building, Hong Kong, China; ykpeng@cityu.edu.hk

<sup>4</sup> Department of Chemistry, ICEx, Universidade Federal de Minas Gerais, Belo Horizonte 31270-901, Brazil; ingridfs@ufmg.br

<sup>5</sup> Department of Chemistry, University of Helsinki, A.I. Virtasen aukio 1, 00100 Helsinki, Finland; jhon.quiroz@helsinki.fi

\* Correspondence: ivo@ufscar.br (I.F.T.); pedro.camargo@helsinki.fi (P.H.C.C.)

Received: 15 July 2020; Accepted: 31 July 2020; Published: 4 August 2020



**Abstract:** Solar-to-chemical conversion via photocatalysis is of paramount importance for a sustainable future. Thus, investigating the synergistic effects promoted by light in photocatalytic reactions is crucial. The tandem oxidative coupling of alcohols and amines is an attractive route to synthesize imines. Here, we unravel the performance and underlying reaction pathway in the visible-light-driven tandem oxidative coupling of benzyl alcohol and aniline employing Au/CeO<sub>2</sub> nanorods as catalysts. We propose an alternative reaction pathway for this transformation that leads to improved efficiencies relative to individual CeO<sub>2</sub> nanorods, in which the localized surface plasmon resonance (LSPR) excitation in Au nanoparticles (NPs) plays an important role. Our data suggests a synergism between the hot electrons and holes generated from the LSPR excitation in Au NPs. While the oxygen vacancies in CeO<sub>2</sub> nanorods trap the hot electrons and facilitate their transfer to adsorbed O<sub>2</sub> at surface vacancy sites, the hot holes in the Au NPs facilitate the  $\alpha$ -H abstraction from the adsorbed benzyl alcohol, evolving into benzaldehyde, which then couples with aniline in the next step to yield the corresponding imine. Finally, cerium-coordinated superoxide species abstract hydrogen from the Au surface, regenerating the catalyst surface.

**Keywords:** tandem; oxidative coupling; Au NPs; CeO<sub>2</sub> nanorods; localized surface plasmon resonance; nanocatalysis

## 1. Introduction

Photocatalysis can initiate or accelerate chemical reactions by the light-matter interaction, which can simultaneously solve the problems about solar energy conversion and storage [1]. Photocatalysts can directly convert solar energy into chemical energy and simultaneously accomplish solar energy conversion and storage objectives [1]. Metal/semiconductor hybrid photocatalysts have emerged as one of the most promising catalytic systems to promote solar-to-chemical conversion. Therefore investigation of the synergistic effects promoted by light in these hybrid photocatalytic systems is of paramount importance for the design of new photocatalysts containing plasmonic

components that can enable improved performance and selectivity via reaction pathways that are not accessible in semiconducting nanoparticles (NPs) or external heating.

The tandem conversion of alcohols into imines, via alcohol oxidation followed by an amine coupling, is of great interest in organic and green chemistry as it can be carried out under mild conditions, alcohols are widely available, and only hydrogen or water are generated as byproducts [2–6]. CeO<sub>2</sub> NPs have been effective as catalysts towards this tandem transformation, where a correlation between oxygen vacancies (as enabled by distinct nanoparticle shapes) and the catalytic activity has been established [6–8]. For instance, CeO<sub>2</sub> nanorods have shown improved performance relative to nanocubes and nanooctahedra due to the exposure of (110) surface facets that enable a greater concentration of oxygen vacancies [7,8].

It has been shown that the nonradiative decay following localized surface plasmon resonance (LSPR) excitation in plasmonic metals leads to hot electrons and holes, that can participate in the electronic or vibrational activation of species close to the surface [9,10]. This provides sufficient energy to initiate, accelerate, and/or control molecular transformations [9,10]. For metals such as Ag, Au, Al, and Cu, the LSPR excitation can take place in the visible range [11,12]. Interestingly, the combination of CeO<sub>2</sub> and plasmonic NPs, such as Au, can provide opportunities for not only achieving improved performance but also opening up reaction pathways under light-excitation that are not accessible via external heating [13–18].

In this work, we unravel the performance and underlying reaction pathway in the visible-light-driven tandem oxidative coupling of benzyl alcohol and aniline employing Au/CeO<sub>2</sub> nanorods as catalysts. We propose an alternative reaction pathway for this transformation that leads to improved efficiencies relative to individual CeO<sub>2</sub> nanorods, in which the LSPR excitation in Au NPs played an important role. Our data suggests a synergism between the hot electrons and holes generated from the LSPR excitation in Au NPs, which acted in combination with the oxygen vacancies in the CeO<sub>2</sub> to improve catalytic activities.

## 2. Experimental Section

### 2.1. Au Nanoparticles Synthesis

Spherical gold nanoparticles with 10–20 nm diameter were synthesized using HAuCl<sub>4</sub>, deionized water, ascorbic acid and polyvinylpyrrolidone (PVP). To a 50 mL round bottom flask were added 6 mL deionized water, 35 mg PVP and 60 mg ascorbic acid, all the solids were dissolved and then the mixture was heated to 90 °C. After 10 min at 90 °C, 1 mL of 3 mmol/L HAuCl<sub>4</sub> solution (5.1 mg in 5 mL of water) was added as fast as possible under intense stirring. After that, the reaction took 3 h at 90 °C and stirring. The obtained Au nanoparticles were washed with 100 mL of water and then suspended in ethanol [19].

### 2.2. Au/CeO<sub>2</sub> Photocatalyst Synthesis

CeO<sub>2</sub> nanorods were synthesized with Ce(NO<sub>3</sub>)<sub>2</sub>·6H<sub>2</sub>O, sodium hydroxide and deionized water. A concentrated NaOH solution was prepared by adding 56 g NaOH into 100 mL deionized water, the solution was cooled to ambient temperature before continuing. After that, 19.9 g Ce(NO<sub>3</sub>)<sub>2</sub>·6H<sub>2</sub>O was added to the NaOH solution and stirred for 30 min, the resultant mixture was transferred into a 150 mL Teflon-lined autoclave and sealed. In order to produce nanorods, the autoclave was kept at 110 °C for 24 h. After that the solution obtained was washed with 1 L deionized water and 100 mL acetone and then transferred to a porcelain crucible, dried at 110 °C for 6 h and calcined for 4 h at 400 °C [20]. Controlled morphology CeO<sub>2</sub> was impregnated with Au nanoparticles using the incipient wetness method. After impregnation, the catalyst was dried at 90 °C overnight and stored.

### 2.3. Catalyst Characterization

Transmission electron microscopy (TEM) images were taken on a JEOL 2100 electron microscope (JEOL, Tokyo, Japan) operating at an accelerating voltage of 200 kV. The samples were prepared to TEM observations by dispersion in ethanol using an ultrasound bath and deposited onto holey-carbon copper grids. The solid-state UV–vis spectra were recorded on a Shimadzu UV-2600 PC spectrophotometer (Shimadzu Corporation, Kyoto, Japan). Wide-angle powder X-Ray Diffraction (XRD) data were recorded in a Rigaku Miniflex diffractometer (Rigaku Corporation, Tokyo, Japan) with Cu K $\alpha$  radiation ( $\lambda = 1.54 \text{ \AA}$ ). The data of  $2\theta$  from 10 to 90° were collected with a step size of 0.02° and acquisition time of 1 s. The diffraction patterns have been indexed by comparison with the Joint Committee on Powder Diffraction Standards (JCPDS) files. The concentrations of Au were determined by atomic absorption spectrometry (AA–Hitachi-Z8200 spectrometer, Hitachi, Japan). The surface area values were obtained by the BET method and the BJH model was used to determine the pore size distributions. The N<sub>2</sub> adsorption and desorption measurements were carried out at 77 K using an Autosorb iQ2 Quantachrome Autosorb Equipment (Quantachrome, Boynton Beach, FL, USA).

### 2.4. Photocatalytic Tests

All the photocatalytic tests were conducted in a 100 mL pressurized photoreactor. In a typical photocatalytic experiment 2.5 mL mesitylene, 80  $\mu\text{L}$  benzyl alcohol, 100  $\mu\text{L}$  aniline, 50 mg catalyst are mixed. With the reactor sealed to prevent solvent evaporation, the catalyst was suspended in an ultrasonic bath and then pressurized with 1 bar O<sub>2</sub>. Except when indicated, all the tests took 48 h at 50 °C with visible spectrum light (300 W) incidence under magnetic stirring. This temperature was chosen based on the best yields reported in the literature for this reaction [21]. The reaction products were analyzed by gas chromatography (GC). Two aliquots (500  $\mu\text{L}$ ) were collected for each reactor batch, the first one before the O<sub>2</sub> loading ( $t = 0$ ) and the second one at the end of the reaction, typically 48h. In both cases, the catalyst was removed by centrifugation (11,000 rpm, 1 min). Both samples were injected in a Shimadzu GC-2010 Plus gas chromatograph. The GC is equipped with a flame ionization detector, which enabled the separation and quantification of all reaction products using an RTX-Wax (30 m  $\times$  0.25 mm  $\times$  0.25  $\mu\text{m}$ ) chromatographic column. The following temperature program was used during the analysis: 50 °C for 3 min; 15 °C min<sup>-1</sup> until 220 °C.

### 2.5. <sup>31</sup>P NMR Measurement of TMP-Adsorbed Samples

A sample of 200 mg of CeO<sub>2</sub> was placed in a glass tube and removed surface adsorbed water at 200 °C for 2 h under vacuum. After cooling down to room temperature, around 300  $\mu\text{mol}$ /catalyst g of trimethylphosphine (TMP) was then introduced. It was allowed around 15 min to reach the steady state for adsorption between TMP and catalyst surface. The sample was then vacuumed at room temperature for 5 min and thus excess non-adsorbed TMP molecules were removed gently without affecting all the chemisorbed peaks. The sample tube was then flame sealed for storage and transferred to Bruker 4mm ZrO<sub>2</sub> rotor with a Kel-F endcap in a glove box under nitrogen atmosphere before NMR characterization. The solid state magic angle spinning (MAS) NMR experiments were carried out using a Bruker Avance III 400WB spectrometer at room temperature. The radiofrequency for decoupling was 59 kHz. The spectral width was 400 ppm, from 200 to –200 ppm. The number of scanings was 800. The <sup>31</sup>P chemical shifts were reported relative to 85% aqueous solution of H<sub>3</sub>PO<sub>4</sub>, with NH<sub>4</sub>H<sub>2</sub>PO<sub>4</sub> as a secondary standard (0.81 ppm).

### 2.6. XPS Analysis

Photoemission studies were conducted in a SPECSLAB II instrument equipped with a Ultra-high vacuum (UHV) chamber where the base pressure was less than  $5 \times 10^{-9}$  Torr. The instrument has a hemispherical electron energy analyzer PHOIBOS-Has 3500 150 with a 9-channels detector operating at 12 kV, pass energy (E<sub>pass</sub>) = 40 eV, 0.2 eV energy step and an Al K $\alpha$  X-ray source. The samples

were placed on stainless steel sample-holders and were placed at the XPS prechamber and held there for 2 h in a vacuum. The collected spectra were adjusted with the CasaXPS 2.3.13 software. The C 1s peak was used as an internal standard for the charge correction (284.5 eV). A Shirley-type background was used [22]. The analysis of the Ce 3d spectra was performed by adjusting 10 components, where 4 components correspond to the Ce<sup>3+</sup> oxidation state (u0, v0, u', v') and the 6 components correspond to the Ce<sup>4+</sup> oxidation state (u, v, u'', v'', u''', v''') [23]. The intensity ratio of Ce 3d<sub>5/2</sub>/Ce 3d<sub>3/2</sub> doublets was set to 1.5 and the energy position was allowed to vary ~2eV around the expected values [24], avoiding the inversion of positions.

### 3. Results and Discussion

The synthesis of Au NPs supported on the CeO<sub>2</sub> nanorods (Au/CeO<sub>2</sub>) was performed by wet impregnation [20]. Figure 1A shows high-resolution transmission electron microscopy (HRTEM) images of the Au/CeO<sub>2</sub> nanorods. The Au NPs presented sizes in the 10–20 nm range. The CeO<sub>2</sub> nanorods were around 10 and 200 nm in width and length, respectively (Figure S1). The Au loading as determined by atomic absorption spectroscopy corresponded to 0.64 wt.%. X-ray diffractometry (Figure S2) showed only peaks assigned to the CeO<sub>2</sub> phase. The UV–vis spectra of the CeO<sub>2</sub> and Au/CeO<sub>2</sub> samples are depicted in Figure 1B (black and red traces, respectively). It can be observed that CeO<sub>2</sub> samples absorb light in the near-visible UV (<450 nm) [8]. Upon Au deposition, a band in the visible (~550 nm) appears due to the LSPR dipolar mode in Au NPs [8,12].

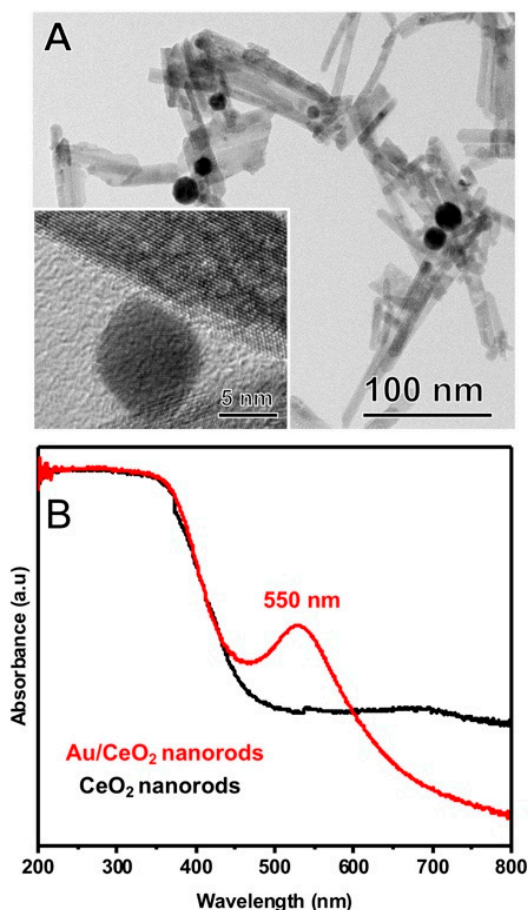


**Figure 1.** (A) HRTEM images for the Au/CeO<sub>2</sub> nanorods. (B) UV–vis extinction spectra for CeO<sub>2</sub> and Au/CeO<sub>2</sub> nanorods (black and red traces, respectively).

Raman and XPS spectroscopies were employed to probe the metal-support interactions and oxygen vacancy properties in CeO<sub>2</sub> and Au/CeO<sub>2</sub> nanomaterials. It is well-known that oxygen vacancies are

structural defects that can adsorb  $O_2$  molecules and are correlated to oxygen mobility and storage capacity [25]. The Raman spectrum of Au/CeO<sub>2</sub> differed from the spectrum of CeO<sub>2</sub> nanorods mainly by the main peak at 450–460  $cm^{-1}$  assigned to oxygen ions vibrational mode in the CeO<sub>2</sub> structure (Figure S3). This peak was strongly broadened in Au/CeO<sub>2</sub>, which was caused by the smaller size of the crystalline domains due to the introduction of Au into the CeO<sub>2</sub> structure. Besides, the Raman mode near 550  $cm^{-1}$  and 600  $cm^{-1}$  assigned to the presence of oxygen vacancies was more intense for Au/CeO<sub>2</sub> relative to the CeO<sub>2</sub> nanorods, in agreement with the Au-CeO<sub>2</sub> metal-support interactions that increased the number of oxygen vacancy sites (Figure S3) [26,27]. This is further confirmed by the Au 4f core-level XPS for Au/CeO<sub>2</sub> nanorods (Figure S4). The Au 4f region showed two photoelectron peaks ascribed to Au 4f<sub>7/2</sub> and Au 4f<sub>5/2</sub> core-levels [12]. These peaks were shifted towards lower BE values, 82.7 and 86.3 eV, respectively, relative to Au in the metallic state [28]. The Ce 3d core-level XPS spectra showed peak positions characteristic of CeO<sub>2</sub> with the presence of Ce<sup>3+</sup> in both CeO<sub>2</sub> and Au/CeO<sub>2</sub> samples (Figure S5, Tables S1 and S2). The BET surface area for the samples CeO<sub>2</sub> and Au/CeO<sub>2</sub> were 86.3  $m^2 \cdot g^{-1}$  and 70.6  $m^2 \cdot g^{-1}$  (Figure S6 and Table S3), respectively. The comparable values evidence that the Au deposition did not affect the CeO<sub>2</sub> nanorods surface area. The same trend was observed for the pore diameter distribution (Figure S7 and Table S3).

We also studied the Au/CeO<sub>2</sub> and CeO<sub>2</sub> nanorods by <sup>31</sup>P-ssNMR analysis employing trimethylphosphine (TMP) as a surface probe. TMP is an electron donor molecule that can specifically form an adduct with surface Ce cation (i.e., TMP-Ce) [29]. In this case, the chemical shift of <sup>31</sup>P is expected to differentiate the strength of the adduct bond formed with various Ce acidities (or electron density) as the stronger surface Lewis acid site pushes  $\delta^{31}P$  to positive ppm [30]. As shown in Figure 2, the <sup>31</sup>P chemical shift of TMP-adsorbed nanorods shifted from 25.7 to 23.5 ppm after Au incorporation, suggesting that the electron density of surface Ce was decreased upon contact with Au. This lower electron density of surface Ce for the Au/CeO<sub>2</sub> nanorods sample might be associated with more oxygen vacancies and more active vacancies [31,32].

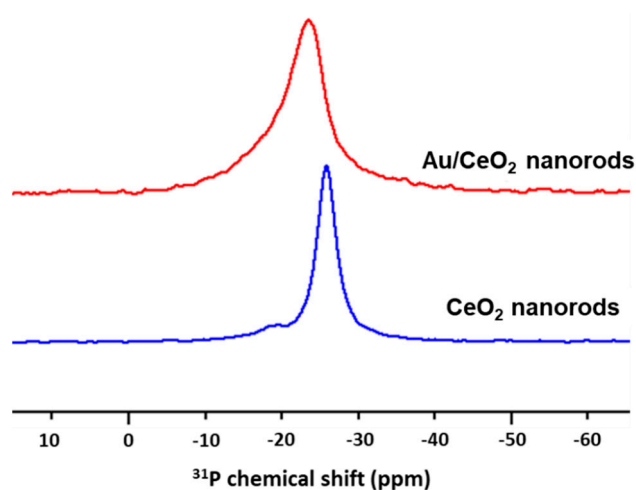


**Figure 2.** <sup>31</sup>P ss NMR spectra of CeO<sub>2</sub> and Au/CeO<sub>2</sub> nanorods (blue and red traces, respectively) using trimethylphosphine (TMP) as a surface probe. After Au deposition, the <sup>31</sup>P NMR signal shifted from 25.7 to 23.5 ppm, suggesting that the electron density of the Ce surface is decreased upon Au deposition.

We then turned our attention to the catalytic activities towards the tandem imine production from alcohols and amines driven by light irradiation. We employed only benzyl alcohol and aniline as substrates [21]. It is accepted that this tandem reaction pathway starts with the alcohol oxidation to aldehyde followed by a spontaneous aldehyde-amine coupling, releasing the active redox site for a new reaction [6]. We employed a white lamp as the irradiation source and started by investigating the activities of the individual Au NPs and CeO<sub>2</sub> nanorods as catalysts as described in Table 1. The use of Au NPs as catalysts showed a very low conversion percentage under light excitation (2.3%, Entry 1),

indicating that the LSPR excitation on Au NPs alone did not significantly contribute to the catalytic activity. The individual CeO<sub>2</sub> nanorods (Table 1, Entries 2 and 3), on the other hand, displayed better activities, reaching around 62–63% conversion both in the dark and under light excitation. The higher activities occurred as a result of the presence of the oxygen vacancies, that acted as active sites for alcohol oxidation [8]. The similar activities detected for dark and light conditions show that the light excitation does not lead to any enhancements in catalytic activity in the CeO<sub>2</sub> nanorods.

**Table 1.** Conversion and selectivity for the tandem conversion of benzyl alcohol into imines as a function of the catalysts and reaction conditions.

Reaction scheme: Benzyl alcohol (1) + Aniline (2) → N-benzylideneaniline (3)

Entry	Catalyst	Conversion of BnOH (%)	Selectivity (%)	
			Imine	Other
1 <sup>a</sup>	Au NPs (Light)	2.3	100	0
2	Nanorods (Light)	62.9	96	4
3	Nanorods (No light)	62.5	97	3
4	Au/nanorods (Light)	91.2	97	3
5	Au/nanorods (No light)	69.5	97	3
6 <sup>d</sup>	Au/nanorods (Light, Ar atmosphere)	31.7	97	3
7 <sup>d</sup>	Au/nanorods (No light, Ar atmosphere)	62.1	97	3
8 <sup>b</sup>	Au/nanorods (Light, electron scavenger)	68.7	97	3
9 <sup>c</sup>	Au/nanorods (Light, hole scavenger)	30.7	97	3

Typical experiment: 1 mmol benzyl alcohol, 2 mmol aniline, 50 mg of catalyst, 1 bar of O<sub>2</sub>, visible light, 50 °C, 48 h; <sup>a</sup> Au NPs colloidal suspension was added in equivalent amount to the Au concentration on Au/CeO<sub>2</sub> samples; <sup>b</sup> 10 mmol benzoquinone (electron scavenger); <sup>c</sup> 10 mmol EDTA (hole scavenger); <sup>d</sup> Inert atmosphere (oxygen gas is replaced by argon).

Interestingly, the incorporation of Au NPs into the CeO<sub>2</sub> nanorods (Au/CeO<sub>2</sub>) led to a significant increase in the catalytic activity under light excitation to 91%, while keeping the selectivity to imines close to 97% (Table 1, Entry 4). In the dark, the activities corresponded to 69.5% (Table 1, Entry 5), which is close to the value detected for the individual CeO<sub>2</sub> nanorods. The results from individual Au NPs (Entry 1) indicated that the enhancement observed for the Au/CeO<sub>2</sub> sample under light irradiation (Entry 4) was not only due to the presence of Au NPs and its plasmonic effects, for example. The observed effect was necessarily due to the synergism between CeO<sub>2</sub> nanorods and the Au NPs, which was responsible for a conversion increment far beyond the sum of the conversion promoted by the CeO<sub>2</sub> nanorods and the Au NPs individual counterparts.

We performed control experiments using electron or hole scavengers (Table 1, Entries 8 and 9) and by replacing the reaction medium with an Ar atmosphere (absence of O<sub>2</sub>) (Table 1, Entries 6 and 7) to better understand the photocatalytic enhancements in Au/CeO<sub>2</sub> nanorods. Under light excitation, the use of an Ar atmosphere decreased the conversion to 31.7% (Entry 6) relative to 91.2% in O<sub>2</sub> (Entry 4). This demonstrates that the O<sub>2</sub> plays a central role in this conversion driven by light. Suppression of catalytic activity was observed under the Ar atmosphere and light excitation relative to the utilization

of the Ar atmosphere and dark conditions (62.1%, Entry 7). Surprisingly, under dark conditions, the conversion in the O<sub>2</sub> and Ar atmosphere was similar (Entries 5 and 7, respectively). This result demonstrates that the presence of O<sub>2</sub> and the plasmonic excitation (light irradiation) are required for the high activities detected for the Au/CeO<sub>2</sub> nanorods (Entry 4).

Based on these results we would like to propose that the unique structure of the (110) surface facets in the CeO<sub>2</sub> nanorods (Figure 3A) allow first the adsorption of benzyl alcohol (via a deprotonation pathway) (Figure 3B). As Tamura and collaborators demonstrated, this deprotonation step does not depend on O<sub>2</sub> [6] and is easily accomplished by the Lewis acid (LA) sites on the CeO<sub>2</sub> (110) surface facet (i.e., Ce<sup>4+</sup> surficial species) [29,33,34]. Even under dark conditions some synergistic effect is observed for the Au/CeO<sub>2</sub>, the Au NPs promotes an increment from 62.5% (Entry 3) to 69.5% (Entry 5) for the imine formation. It is well-established for alcohol oxidation investigations (not light-driven) that this synergistic effect occurs due to the charge separation in the interface Au/CeO<sub>2</sub>, in which the Au NPs gives an e<sup>-</sup> for the Ce<sup>4+</sup> reducing it to Ce<sup>3+</sup> and the Au NPs keep the positive charge [33,35]. These positive-charged Au species are responsible for the C-H activation, which is the limiting step of the reaction [33,35]. Under light irradiation, this synergistic effect, due to the charge separation, is further promoted. Upon LSPR excitation of the Au NPs, hot electrons and hot holes are generated [13,14]. The hot electrons can be trapped at the redox sites of the CeO<sub>2</sub> while the hot holes remain at the Au NPs (Figure 3C and Figure S8). The electrons in the CeO<sub>2</sub> will reduce some Ce<sup>4+</sup> into Ce<sup>3+</sup> generating vacancies (Figure 3C). In the next step, hot holes on Au NPs can contribute to the α-H abstraction from the adsorbed benzyl alcohol substrate leading to a carbon-centered radical (Figure 3C,D) and H-Au species over the Au NP [35–37]. These H-Au species were trapped by 5,5-dimethyl-1-pyrroline *N*-oxide (DMPO) in electron paramagnetic resonance (EPR) experiments reported by Garcia et al. under similar conditions [35]. Simultaneously, trapped hot electrons can be transferred to O<sub>2</sub> species adsorbed on vacancies to give surface-bound •O<sub>2</sub><sup>-</sup> (Figure 3C,D). We then hypothesize that the carbon-centered radical can recombine with the electrons trapped on the vacancies (Ce<sup>3+</sup> species) regenerating the Ce<sup>4+</sup> and forming benzaldehyde, which couples with the aniline enabling the tandem formation of the imines. The cerium-coordinated superoxide species have the important role of regenerating the surface of Au NPs by hydrogen abstraction from H-Au (Figure 3E), leading to H<sub>2</sub>O<sub>2</sub> [33]. By replacing O<sub>2</sub> with an inert atmosphere, there is a decrease in the conversion percentage as no O<sub>2</sub> is available to regenerate the Au surface. The deactivation of the Au surface in the absence of an oxidant can be noticed by comparing the reactions for the Au/nanorods sample under Ar (Entry 7) and nanorods (no Au) without irradiation under O<sub>2</sub> (Entry 2), both display similar activities (62.1% and 62.9%, respectively), which are lower than the Au/nanorods sample under O<sub>2</sub> (Entry 7). Garcia et al. reported that this reaction can be performed in the absence of O<sub>2</sub> when DMPO is used to abstract the H-Au species and regenerate the Au NPs [35]. Therefore, it is plausible that in the absence of an oxidant, chemisorbed hydrogens stay bonded to the Au NPs surface, poisoning its surface. This is supported by the chromatogram for the reaction products in the absence of O<sub>2</sub>, which displayed the same profile and no amines were detected.

In the absence of O<sub>2</sub> and under light the catalyst activity is suppressed, reaching smaller values relative to the reaction in the dark (both in the presence of O<sub>2</sub> and Ar atmosphere). It is plausible that hot electrons trapped at the oxygen vacancy sites are not transferred to adsorbed O<sub>2</sub>. Instead, they can be transferred to the adsorbed benzyl alcohol species disfavoring the α-H abstraction and suppressing the reaction rates. Under dark conditions, the LSPR excitation does not play a role in this transformation and activities under Ar and O<sub>2</sub> yield similar results. Thus, in the absence of light excitation, the O<sub>2</sub> plays an even more important role over the benzyl alcohol oxidation.

This proposed reaction pathway is also supported by the conversion percentage for the Au/CeO<sub>2</sub> nanorods in the presence of electrons or hole scavengers (under light excitation and O<sub>2</sub> atmosphere). In the presence of electron scavengers, adsorbed O<sub>2</sub> species activation is disfavored and the resulting activities are similar for the Au/CeO<sub>2</sub> nanorods under dark conditions and CeO<sub>2</sub> nanorods. In this case, activities are dictated by the CeO<sub>2</sub> redox sites. In the presence of hole scavengers, the α-H abstraction from the adsorbed benzyl alcohol substrate is suppressed, and conversion percentages decrease to

30.7%. Hole scavengers can deactivate the positive charged Au species as well as the CeO<sub>2</sub> redox sites, both active sites present in the catalyst. This result suggests that the synergistic effect is taking place through a charge separation process and not only by a heating effect promoted by the Au NPs. The possibility of a reaction between EDTA (hole scavenger) and the reactants was excluded by the absence of new peaks in the GC-MS analysis. Under Ar atmosphere, activity suppression is also observed, this effect is related to the deactivation of the Au surface, once •O<sub>2</sub><sup>-</sup> formation is avoided and the catalyst surface is not regenerated. Furthermore, the absence of O<sub>2</sub> or electron receptor species might influence the Ce<sup>3+</sup>/Ce<sup>4+</sup> ratio, leading to a deactivation of the redox sites of the CeO<sub>2</sub> [6].

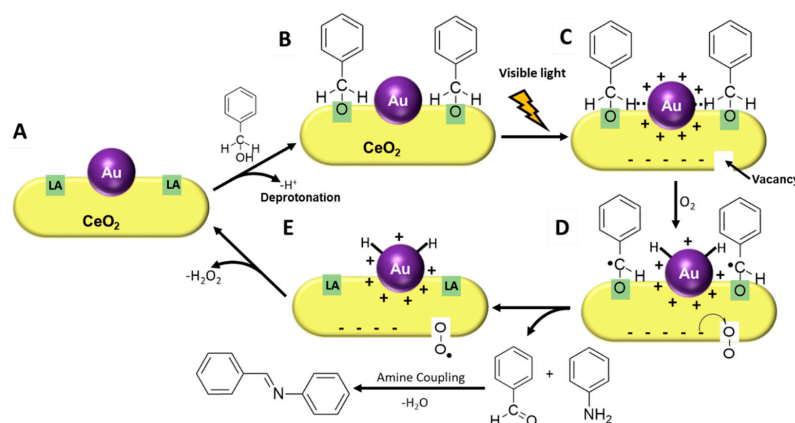


**Figure 3.** Schematic representation of the proposed photocatalytic mechanism. The LA sites (A) enable the adsorption of benzyl alcohol (B), via a deprotonation pathway. Localized surface plasmon resonance (LSPR) excitation leads to the formation of hot electrons and holes (C). Hot electrons get trapped at vacancy sites, where they activate adsorbed O<sub>2</sub> (C,D). Hot holes facilitate the  $\alpha$ -H abstraction from the adsorbed benzyl alcohol (C,D). The cerium-coordinated superoxide species can abstract hydrogen from H-Au species (E), regenerating the catalyst surface. The formed benzaldehyde couples with aniline in the next step to generate the imine.

#### 4. Conclusions

In summary, we have demonstrated that the plasmonic excitation in Au/CeO<sub>2</sub> nanorods enables an alternative reaction pathway that leads to improved catalytic performance relative to individual CeO<sub>2</sub> nanorods towards the visible-light-driven tandem synthesis of imines via alcohol oxidation. Our results demonstrated that the presence of O<sub>2</sub>, oxygen vacancies in CeO<sub>2</sub>, and both hot electrons and holes generated as a result of LSPR excitation in the visible range were crucial to the detected photocatalytic performances. While the hot electrons lead to the formation of oxygen vacancies, enabling the adsorption of O<sub>2</sub>, hot holes generate positive-charged Au species, which facilitate the  $\alpha$ -H abstraction from the adsorbed benzyl alcohol. The produced carbon-centered radical can recombine with the electrons trapped in the vacancies producing the benzaldehyde, which couples with the aniline, enabling the tandem formation of the imines. The cerium-coordinated superoxide regenerates the surface of Au NPs by hydrogen abstraction, forming H<sub>2</sub>O<sub>2</sub>. We believe the results presented herein can inspire the development of photocatalysts containing plasmonic components that can enable improved performance and selectivity via reaction pathways that are not accessible in semiconducting NPs or external heating.

**Supplementary Materials:** The following are available online at <http://www.mdpi.com/2079-4991/10/8/1530/s1>, Figure S1: TEM CeO<sub>2</sub> nanorods, Figure S2: XRD, Figure S3: Raman spectra, Figure S4 and S5: XPS spectra, Table S1: Binding energies Au 4f XPS, Table S2: Binding energies O 1s XPS, Figure S6: Isotherms BET, Figure S7: BJH pore diameter distribution, Table S3: BET surface area and average pore diameter, Figure S8: Scheme of the energy level diagram for the Au/CeO<sub>2</sub> nanorod photocatalyst.

**Author Contributions:** Conceptualization, I.F.T., R.S.G. and P.H.C.C.; methodology, I.F.T., R.S.G., M.S.H. and P.H.C.C.; XPS analysis, J.Q.; BET analysis, I.F.S.; <sup>31</sup>P NMR, Y.-K.P.; investigation, I.F.T., M.S.H., R.S.G., G.F.S.R.R., Y.-K.P., I.F.S. J.Q. and P.H.C.C.; resources, I.F.T., M.S.H., R.S.G., G.F.S.R.R., Y.-K.P., I.F.S. J.Q. and P.H.C.C.;

data curation, I.F.T. and M.S.H.; writing—original draft preparation, I.F.T. and P.H.C.C.; writing—review and editing, I.F.T., I.F.S. and P.H.C.C.; supervision, I.F.T. and P.H.C.C.; project administration, P.H.C.C.; funding acquisition, P.H.C.C. All authors have read and agreed to the published version of the manuscript.

**Funding:** This research was funded by CAPES, CNPq and FAPESP (grant numbers 423196/2018-9 and 2017/50118-9).

**Acknowledgments:** P.H.C.C. thanks the Jane and Aatos Erkkö Foundation and the University of Helsinki for financial support.

**Conflicts of Interest:** The authors declare no conflict of interest.

## References

1. Wang, F.; Li, Q.; Xu, D. Recent Progress in Semiconductor-Based Nanocomposite Photocatalysts for Solar-to-Chemical Energy Conversion. *Adv. Energy Mater.* **2017**, *7*, 1700529. [[CrossRef](#)]
2. Parsons, P.J.; Penkett, C.S.; Shell, A.J. Tandem reactions in organic synthesis: Novel strategies for natural product elaboration and the development of new synthetic methodology. *Chem. Rev.* **1996**, *96*, 195–206. [[CrossRef](#)]
3. Anastas, P.T.; Warner, J.C. Principles of green chemistry. In *Green Chemistry Theory and Practice*; Oxford University Press: New York, NY, USA, 1998; pp. 29–56.
4. Behr, A.; Vorholt, A.J.; Ostrowski, K.A.; Seidensticker, T. Towards resource efficient chemistry: Tandem reactions with renewables. *Green Chem.* **2014**, *16*, 982–1006. [[CrossRef](#)]
5. Patil, R.D.; Adimurthy, S. Catalytic methods for imine synthesis. *Asian J. Org. Chem.* **2013**, *2*, 726–744. [[CrossRef](#)]
6. Tamura, M.; Tomishige, K. Redox properties of CeO<sub>2</sub> at low temperature: The direct synthesis of imines from alcohol and amine. *Angew. Chem. Int. Ed.* **2015**, *54*, 864–867. [[CrossRef](#)]
7. Zhang, J.; Yang, J.; Wang, J.; Ding, H.; Liu, Q.; Schubert, U.; Rui, Y.; Xu, J. Surface oxygen vacancies dominated CeO<sub>2</sub> as efficient catalyst for imine synthesis: Influences of different cerium precursors. *Mol. Catal.* **2017**, *443*, 131–138. [[CrossRef](#)]
8. Montini, T.; Melchionna, M.; Monai, M.; Fornasiero, P. Fundamentals and catalytic applications of CeO<sub>2</sub>-based materials. *Chem. Rev.* **2016**, *116*, 5987–6041. [[CrossRef](#)]
9. Araújo, T.P.; Quiroz, J.; Barbosa, E.M.; Camargo, P.H.C. Understanding plasmonic catalysis with controlled nanomaterials based on catalytic and plasmonic metals. *Curr. Opin. Colloid Interface Sci.* **2019**, *39*, 110–122.
10. Wang, J.; Ando, R.A.; Camargo, P.H.C. Controlling the Selectivity of the Surface Plasmon Resonance Mediated Oxidation of p-Aminothiophenol on Au Nanoparticles by Charge Transfer from UV-excited TiO<sub>2</sub>. *Angew. Chem. Int. Ed.* **2015**, *54*, 6909–6912. [[CrossRef](#)]
11. Rodrigues, T.S.; da Silva, A.G.M.; Camargo, P.H.C. Nanocatalysis by noble metal nanoparticles: Controlled synthesis for the optimization and understanding of activities. *J. Mater. Chem. A* **2019**, *7*, 5857–5874. [[CrossRef](#)]
12. Geonmonond, R.S.; Quiroz, J.; Rocha, G.F.S.R.; Oropeza, F.E.; Rangel, C.J.; Rodrigues, T.S.; Hofmann, J.P.; Hensen, E.J.M.; Ando, R.A.; Camargo, P.H.C. Marrying SPR excitation and metal-support interactions: Unravelling the contribution of active surface species in plasmonic catalysis. *Nanoscale* **2018**, *10*, 8560–8568. [[CrossRef](#)]
13. Zhu, K.; Wang, C.; Camargo, P.H.C.; Wang, J. Investigating the effect of MnO<sub>2</sub> band gap in hybrid MnO<sub>2</sub>-Au materials over the SPR-mediated activities under visible light. *J. Mater. Chem. A* **2019**, *7*, 925–931. [[CrossRef](#)]
14. Wang, J.; de Freitas, I.C.; Alves, T.V.; Ando, R.A.; Fang, Z.; Camargo, P.H.C. On the effect of native SiO<sub>2</sub> on Si over the SPR-mediated photocatalytic activities of Au and Ag nanoparticles. *Chem. Eur. J.* **2017**, *23*, 7185–7190. [[CrossRef](#)]
15. Haruta, M.; Daté, M. Advances in the catalysis of Au nanoparticles. *Appl. Catal. A Gen.* **2001**, *222*, 427–437. [[CrossRef](#)]
16. Coquet, R.; Howard, K.L.; Willock, D.J. Theory and simulation in heterogeneous gold catalysis. *Chem. Soc. Rev.* **2008**, *37*, 2046–2076. [[CrossRef](#)]
17. Dhakshinamoorthy, A.; Asiri, A.M.; Garcia, H. Metal organic frameworks as versatile hosts of Au nanoparticles in heterogeneous catalysis. *ACS Catal.* **2017**, *7*, 2896–2919. [[CrossRef](#)]
18. Shahzad, S.A.; Sajid, M.A.; Khan, Z.A.; Canseco-Gonzalez, D. Gold catalysis in organic transformations: A review. *Synth. Commun.* **2017**, *47*, 735–755. [[CrossRef](#)]

19. Damato, T.C.; de Oliveira, C.C.S.; Ando, R.M.A.; Camargo, P.H.C. A facile approach to TiO<sub>2</sub> colloidal spheres decorated with Au nanoparticles displaying well-defined sizes and uniform dispersion. *Langmuir* **2013**, *29*, 1642–1649. [[CrossRef](#)]
20. Si, R.; Flytzani-Stephanopoulos, M. Shape and crystal-plane effects of nanoscale ceria on the activity of Au-CeO<sub>2</sub> catalysts for the water–gas shift reaction. *Angew. Chem. Int. Ed.* **2008**, *47*, 2884–2887. [[CrossRef](#)]
21. Zhang, Z.; Wang, Y.; Wang, M.; Lü, J.; Li, L.; Zhang, Z.; Li, M.; Jiang, J.; Wang, F. An investigation of the effects of CeO<sub>2</sub> crystal planes on the aerobic oxidative synthesis of imines from alcohols and amines. *Chin. J. Catal.* **2015**, *36*, 1623–1630. [[CrossRef](#)]
22. Shirley, D.A. High-resolution X-ray photoemission spectrum of the valence bands of gold. *Phys. Rev. B* **1972**, *5*, 4709. [[CrossRef](#)]
23. Burroughs, P.; Hamnett, A.; Orchard, A.F.; Thornton, G. Satellite structure in the X-ray photoelectron spectra of some binary and mixed oxides of lanthanum and cerium. *J. Chem. Soc. Dalton Trans.* **1976**, 1686–1698. [[CrossRef](#)]
24. Maslakov, K.I.; Teterin, Y.A.; Popel, A.J.; Teterin, A.Y.; Ivanov, K.E.; Kalmykov, S.N.; Petrov, V.G.; Petrov, P.K.; Farnan, I. XPS study of ion irradiated and unirradiated CeO<sub>2</sub> bulk and thin film samples. *Appl. Surf. Sci.* **2018**, *448*, 154–162. [[CrossRef](#)]
25. Zhao, K.; Qi, J.; Yin, H.; Wang, Z.; Zhao, S.; Ma, X.; Wan, J.; Chang, L.; Gao, Y.; Yu, R. Efficient water oxidation under visible light by tuning surface defects on ceria nanorods. *J. Mater. Chem. A* **2015**, *3*, 20465–20470. [[CrossRef](#)]
26. Li, J.; Liu, X.; Zhan, W.; Guo, Y.; Guo, Y.; Lu, G. Preparation of high oxygen storage capacity and thermally stable ceria-zirconia solid solution. *Catal. Sci. Technol.* **2016**, *6*, 897–907. [[CrossRef](#)]
27. Kalamaras, C.M.; Petalidou, K.C.; Efstathiou, A.M. The effect of La<sup>3+</sup>-doping of CeO<sub>2</sub> support on the water-gas shift reaction mechanism and kinetics over Pt/Ce<sub>1-x</sub>La<sub>x</sub>O<sub>2-δ</sub>. *Appl. Catal. B Environ.* **2013**, *136*, 225–238. [[CrossRef](#)]
28. Casaletto, M.P.; Longo, A.; Martorana, A.; Prestianni, A.; Venezia, A.M. XPS study of supported gold catalysts: The role of Au<sup>0</sup> and Au<sup>+δ</sup> species as active sites. *Surf. Interface Anal.* **2006**, *38*, 215–218. [[CrossRef](#)]
29. Tan, Z.; Li, G.; Chou, H.-L.; Li, Y.; Yi, X.; Mahadi, A.H.; Zheng, A.; Tsang, S.C.E.; Peng, Y.-K. Differentiating Surface Ce Species Among CeO<sub>2</sub> Facets by Solid-State NMR for Catalytic Correlation. *ACS Catal.* **2020**, *10*, 4003–4011. [[CrossRef](#)]
30. Zheng, A.; Liu, S.-B.; Deng, F. <sup>31</sup>P NMR chemical shifts of phosphorus probes as reliable and practical acidity scales for solid and liquid catalysts. *Chem. Rev.* **2017**, *117*, 12475–12531. [[CrossRef](#)]
31. Kim, H.Y.; Lee, H.M.; Henkelman, G. CO oxidation mechanism on CeO<sub>2</sub>-supported Au nanoparticles. *J. Am. Chem. Soc.* **2012**, *134*, 1560–1570. [[CrossRef](#)] [[PubMed](#)]
32. Song, W.; Hensen, E.J.M. Mechanistic aspects of the water–gas shift reaction on isolated and clustered Au atoms on CeO<sub>2</sub> (110): A density functional theory study. *ACS Catal.* **2014**, *4*, 1885–1892. [[CrossRef](#)]
33. Abad, A.; Concepción, P.; Corma, A.; García, H. A collaborative effect between gold and a support induces the selective oxidation of alcohols. *Angew. Chem. Int. Ed.* **2005**, *44*, 4066–4069. [[CrossRef](#)] [[PubMed](#)]
34. Tamura, M.; Tomishige, K. Scope and reaction mechanism of CeO<sub>2</sub>-catalyzed one-pot imine synthesis from alcohols and amines. *J. Catal.* **2020**, *389*, 285–296. [[CrossRef](#)]
35. Maldotti, A.; Molinari, A.; Juárez, R.; Garcia, H. Photoinduced reactivity of Au-H intermediates in alcohol oxidation by gold nanoparticles supported on ceria. *Chem. Sci.* **2011**, *2*, 1831–1834. [[CrossRef](#)]
36. Conte, M.; Miyamura, H.; Kobayashi, S.; Chechik, V. Spin trapping of Au-H intermediate in the alcohol oxidation by supported and unsupported gold catalysts. *J. Am. Chem. Soc.* **2009**, *131*, 7189–7196. [[CrossRef](#)]
37. Li, H.; Qin, F.; Yang, Z.; Cui, X.; Wang, J.; Zhang, L. New reaction pathway induced by plasmon for selective benzyl alcohol oxidation on BiOCl possessing oxygen vacancies. *J. Am. Chem. Soc.* **2017**, *139*, 3513–3521. [[CrossRef](#)]

